



Effect of Fe and Mn Content on the Microstructures and Tensile Behaviour of AlSi7Cu3 Alloy: Thermal Analysis and Tensile Tests

Zaidao Li^{1,2} · Nathalie Limodin¹ · Amina Tandjaoui¹ · Philippe Quaegebeur¹ · Xiangzhen Zhu³ · David Balloy²

Received: 23 August 2021 / Accepted: 1 October 2021 / Published online: 16 April 2022
© The Korean Institute of Metals and Materials 2022

Abstract

The present study was performed on two AlSi7Cu3 alloys with different Fe and Mn contents (standard alloy and high-Fe/Mn alloy). The evolution of microstructures during solidification of the standard AlSi7Cu3 alloy was investigated by thermal analysis and interrupted quenching test. The effect of Fe and Mn content on the solidification reaction and sequence were studied. The results show that increasing the Fe and Mn content changes the precipitation sequence of the iron-intermetallic α -Al₁₅(Fe,Mn)₃Si₂ and β -Al₃FeSi, leading to the precipitation of $\alpha + \beta$ phases at a higher temperature. Microstructural characterizations were also performed on the fully solidified alloys to study the effect of Fe and Mn content on the microstructure of AlSi7Cu3 alloy. Fe and Mn were found to promote the formation of Fe-intermetallics. With the increase of Fe/Mn content, Fe-intermetallics increased in both size and amount, while more small pores (Feret diameter < 200 μ m) were also introduced. 3D networks of α -Al₁₅(Fe,Mn)₃Si₂ and β -Al₃FeSi phases were revealed by Lab X-ray Computed Tomography, however, it is difficult to perform a quantitative analysis of the respective volume fraction of α -Al₁₅(Fe,Mn)₃Si₂ and β -Al₃FeSi phase from their 3D morphology. Monotonic tensile tests on both alloys show the mechanical properties of the studied alloys were not sensitive to the Fe/Mn content, while the fractography analysis reveals that cracks growth and final fracture under monotonic load are more prone to occur through the eutectic Si, Al₂Cu phases and iron-intermetallics than through aluminium matrix.

Keywords Al-Si-Cu alloys · Thermal analysis · Fe-rich intermetallics · Fe/Mn content · Tomography · Fractography

1 Introduction

Aluminum–silicon casting alloys are widely used in the automotive industry because of their low cost, light weight and acceptable mechanical properties [1]. Among the commercial aluminum–silicon casting alloys, A319 (AlSi7Cu3) alloy is commonly used for car cylinder heads and has been receiving increased interest due to the balance of properties

that can be achieved using suitable heat treatments [2]. Solidification plays an important role in affecting the microstructure and hence influencing the mechanical properties and quality of cast products [3]. Therefore, it is important to develop an understanding of the mechanisms of solidification for AlSi7Cu3 alloy and of how the resulting microstructure is affected by parameters such as temperature and alloy composition.

Iron is probably the most detrimental element and exists as a common impurity element in Al–Si alloys, especially in recycled aluminium alloy [4]. During solidification process, iron, together with other alloying elements (Cu, Mg, Zn, Mn, Ti, etc.) partly goes into solid solution in the matrix and partly forms Fe-rich intermetallic particles [5]. In Al–Si–Cu alloy, the common iron-intermetallics are β -Al₃FeSi and α -Al₁₅(Fe,Mn)₃Si₂ phase, and several researchers [6–8] reported that β -Al₃FeSi phase and α -Al₁₅(Fe,Mn)₃Si₂ phase appear needles-like and Chinese-script in 2D observation, respectively. The β phase is reported to be quite deleterious to the alloy properties due to its brittle nature. Under conditions of high stress intensity factor, the β -platelets fracture or

✉ Zaidao Li
lizaidao@gmail.com

✉ David Balloy
david.balloy@univ-lille.fr

¹ UMR 9013 - LaMcube - Laboratoire de Mécanique, Multiphysique, Multiéchelle, CNRS, Centrale Lille, University Lille, 59000 Lille, France

² UMR 8207 - UMET - Unité Matériaux Et Transformations, CNRS, INRA, ENSCL, University Lille, 59000 Lille, France

³ Brunel Centre for Advanced Solidification Technology (BCAST), Brunel University London, Uxbridge UB8 3PH, UK

separate from the matrix, providing preferential crack paths ahead of the advancing crack, thereby lowering the impact properties of alloys [9]. Some studies [5, 7, 10] reported that the addition of manganese (Mn) can reduce the detrimental effects of the β phase by replacing it with the less-detrimental Chinese script α -Al₁₅(Fe,Mn)₃Si₂ phase. However, the effect of α and β phases morphology on the damage of Al-Si-Cu alloy appears to be little understood, thus, the three-dimensional α and β phases morphology would appear to be particularly important to characterize.

In addition, Dinnis et al. [11] reported that high iron content have a significant effect on the formation of porosity in Al-Si-Cu alloys. Moustafa [4] found that the porosity content increases with the increasing the iron content; Taylor et al. [12, 13] indicated that an intermediate iron content could lead to a minimum level of porosity, and they suggested that the mechanism by which iron causes porosity in the AA309 alloy may be related to the solidification sequence of the alloy.

The aim of the present work was to better understand the microstructure developed with different Fe and Mn content during solidification. Thus, thermal analyses coupled with microstructure observation were performed on two AlSi7Cu3 alloys with different Fe and Mn contents (standard alloy & high-Fe/Mn alloy). Microstructure characterization was performed in order to study the effect of Fe and Mn content on the solidification reaction and microstructures of AlSi7Cu3 alloy using optical- and Scanning Electron Microscopy (SEM) and laboratory X-ray tomography. Besides, the effect of this variation of microstructures, which stems from different Fe/Mn content, on the mechanical and fracture behaviour was also studied.

2 Experimental Procedures

2.1 Materials

The two experimental alloys used in this work are AlSi7Cu3 base alloys obtained from PSA Peugeot Citroën. The “standard” alloy is the commercial chemical composition used for the cylinder heads at PSA. This alloy was modified by addition of Al–25%Fe and Al–25%Mn master alloys to prepare the “high-Fe/Mn” alloy. The compositions of the two experimental alloys were measured using a mass spectrometer and the results are given in Table 1.

2.2 Thermal Analysis

The alloys were melted in a ceramic crucible of 60 mm in diameter by 120 mm in height. This crucible was taken out of the furnace after the alloy has melted, then put into another bigger crucible of 100 mm in diameter by 150 mm in height which was filled with rock wool in order to obtain a low cooling rate. A high sensitivity thermocouple of K type was used to record the temperature at the center of the mould; a support was used to fix the top of the thermocouple to assure that it remained in place during cooling. Data were acquired by a high-speed data acquisition system (PICOLOG) linked to a computer.

Before all temperature measurements, the thermocouples were calibrated at the solidification point of pure aluminium (660 °C) to ensure accurate and precise reading.

In order to reveal and clarify the solidification sequence of the alloys, the interrupted quenching method, i.e. interrupting the solidification process and quenching the solidifying sample into water, was carried out. This method has been previously proven to work by [14]. Samples were quenched at different temperatures and the “water-quenched” structure was then compared with the “normally solidified” structure. The solidification process of the alloy could be revealed and the solidification sequence and microstructure could be determined.

2.3 Microstructural Characterization

Metallographic analysis of the thermal analysis test samples was performed with OM/SEM/EDS to verify the nature of the phases formed. Thus, after thermal analysis, each sample was sectioned horizontally where the tip of the thermocouple was located, and it was prepared by standard grinding and polishing procedures. In this work, the 2D microstructure observations were performed using a Nikon YM-EPI light microscope equipped with a Sony color video camera and a JEOL 7800 F LV SEM. EDS analyses were done using the equipped OXFORD System Aztec and an X-Max 80 mm² premium spectrometer Microanalysis System to identify the morphology and stoichiometry of the intermetallic phases.

X-ray Computed Tomography (CT), which allows the non-destructive 3D characterization of microstructural constituents of a material, is now an established technique in material science. Thus, in the present work, in order to quantitatively characterize the distribution and size of the pores in 3D, cylindrical specimens with 4 mm length and 4 mm diameter

Table 1 Chemical compositions of the experimental AlSi7Cu3 alloys (wt%)

Alloy	Al	Si	Cu	Fe	Mn	Mn/Fe	Sr	Mg	Ti	Pb	Zn
Standard	bal	7.66	3.67	0.49	0.13	0.26	0.012	0.31	0.11	0.05	0.33
High Fe/Mn	bal	7.00	3.45	0.80	0.51	0.64	0.010	0.28	0.12	0.05	0.24

were extracted by CNC equipment between the thermocouple tip and the thermal analysis sample surface, then they were scanned with X-ray tomography with a voxel size of $3.14\ \mu\text{m}$ in a large volume of material: $1200 \times 1200 \times 2500$ voxels, i.e. about $87.5\ \text{mm}^3$.

In order to reveal the intermetallic compounds clearly and obtain high quality tomography images, a high resolution is necessary. Thus, Lab-CT was carried out at a voxel size of $1.1\ \mu\text{m}$ to characterize the Fe-rich intermetallics and Al_2Cu phase. The analyzed cylindrical specimens with 4 mm in length and 1 mm in diameter were extracted from the same location as the large 3D analysis samples; the scanned volume is $1300 \times 1300 \times 2000$ voxels, i.e. about $3.5\ \text{mm}^3$.

Because Al and Si have close atomic numbers hence similar X-ray attenuation, 3D characterization for the Si phase could not be achieved with Lab-CT. However, optical microscopy at a pixel size of $0.7\ \mu\text{m}$ gives enough contrast between the eutectic silicon and Al matrix, thus 2D metallographic analysis was used to characterize the eutectic Si. An average area of about $5.0\ \text{mm}^2$ was selected and examined for both samples so as to represent the features of the whole sample.

2.4 Image Processing

The obtained 2D and 3D images were processed and analyzed using ImageJ/Fiji and Avizo Fire softwares, respectively. For more details about the image processing please refer to [10], the main parameters used to characterize the morphology of intermetallics, Si particles and pores are Feret diameter and local curvature. Feret diameter can be defined as the longest distance measured between two parallel tangents on each side of the 2D or 3D object of interest [15]. Feret diameter was used to assess the size of either pores or hard inclusions as it could better reflect the size of objects with such complex shape. The Mean curvature H is defined as: $H = 0.5 \times (1/R_1 + 1/R_2)$, and the Gaussian curvature K is defined as $K = 1/R_1 \times 1/R_2$, where R_1 and R_2 are the two principal radii of curvature of the surface [16]. The characteristic morphologies, which depend on the different Mean and Gaussian curvature value, can fall into six basic classes: convex, concave, flat, peak, pit and saddle morphologies [17]. The characteristic morphologies for the axes and for each quadrant are indicated schematically in Fig. 1. Local curvature is an important shape parameter for the morphology of the phases. The characterization of 3D shape evolution of dendritic microstructures with local curvatures was studied by Voorhees [18]. Following his pioneering work, Kuijpers et al. [19] studied the evolution of the 3D intermetallic structure in a 6005A aluminium alloy during a homogenization treatment by using local curvature distribution.

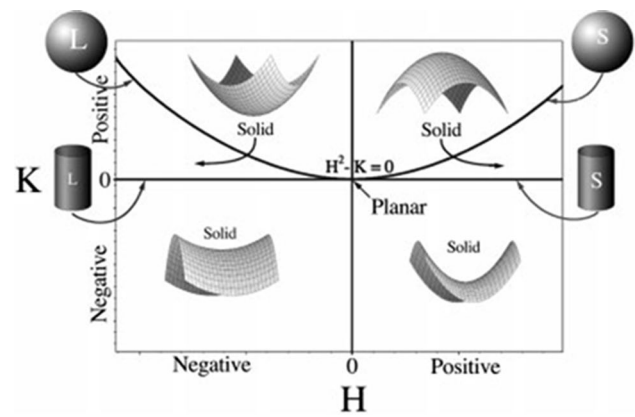


Fig. 1 Map of local surface shapes in H–K space [18]

2.5 Mechanical and Fracture Behaviour

In order to avoid the large gas porosities that could result in early tensile failure and to focus the study on the effect of Fe-intermetallics on the mechanical properties, the melted alloys in the crucible were properly degassed. After the full solidification, tensile samples were machined as per ASTM E-8 sub-size specifications (dimensions: 3 mm in thickness, 6 mm in width, 25 mm in gauge length). The tensile tests were carried out with a displacement rate of $0.36\ \text{mm/min}$ on both alloys (“standard” alloy and high-Fe/Mn alloy) on an Instron 5500 machine; strain was measured using a 25 mm gauge length extensometer. The mechanical properties of the alloys were evaluated using at least three tensile specimens. Fracture surface characterization studies were performed on the tensile fractured samples by a JEOL scanning electron microscope equipped with EDS.

3 Results

3.1 Thermal Analysis

Thermal Analysis method is commonly used to determine a full range of solidification features for aluminium alloys [14]. The temperature changes in the sample from a liquid to a solidified state during cooling are recorded. The slope of cooling curve can reflect the release of latent heat of solidification, and this can be used to detect the phase reactions and characteristics of transformations during solidification [20]. In this part, thermal analyses coupled with microstructure observation were performed on the two studied alloys (see Table 1). The evolution of microstructures during solidification of the standard Al-Si-Cu alloy and the effect of high Fe and Mn content on the solidification reaction of Al-Si-Cu alloy were studied.

3.1.1 Solidification Reaction and Sequence of the Al-Si-Cu Alloy

Figure 2 shows the cooling curve and its first derivative, with an average cooling rate of approximately 0.13 °C/s, obtained during the solidification of the standard alloy, which is the standard chemical composition used for the cylinder heads at PSA. Five peaks were observed in the first derivative curve, marked 1 to 5, which correspond to thermal events that occurred during solidification of the alloy.

In order to determine whether these peak-like fluctuations are associated with precipitation of any phase and to

link the peaks to reactions that happened during solidification, a series of interrupted water-quenching test were performed at different stages of the solidification of the standard alloy. Subsequent observation by OM and SEM–EDS of the quenched microstructures is performed to study the solidification reactions and sequence.

The yellow points, i.e. from (a) to (f), in the first derivative curve represent the quench tests performed on the sample, and the corresponding metallographic microstructures are shown in Fig. 2a–f.

In the sample quenched at 560 °C, only Al dendrites were observed in Fig. 2a, thus the first solid phase formed is the

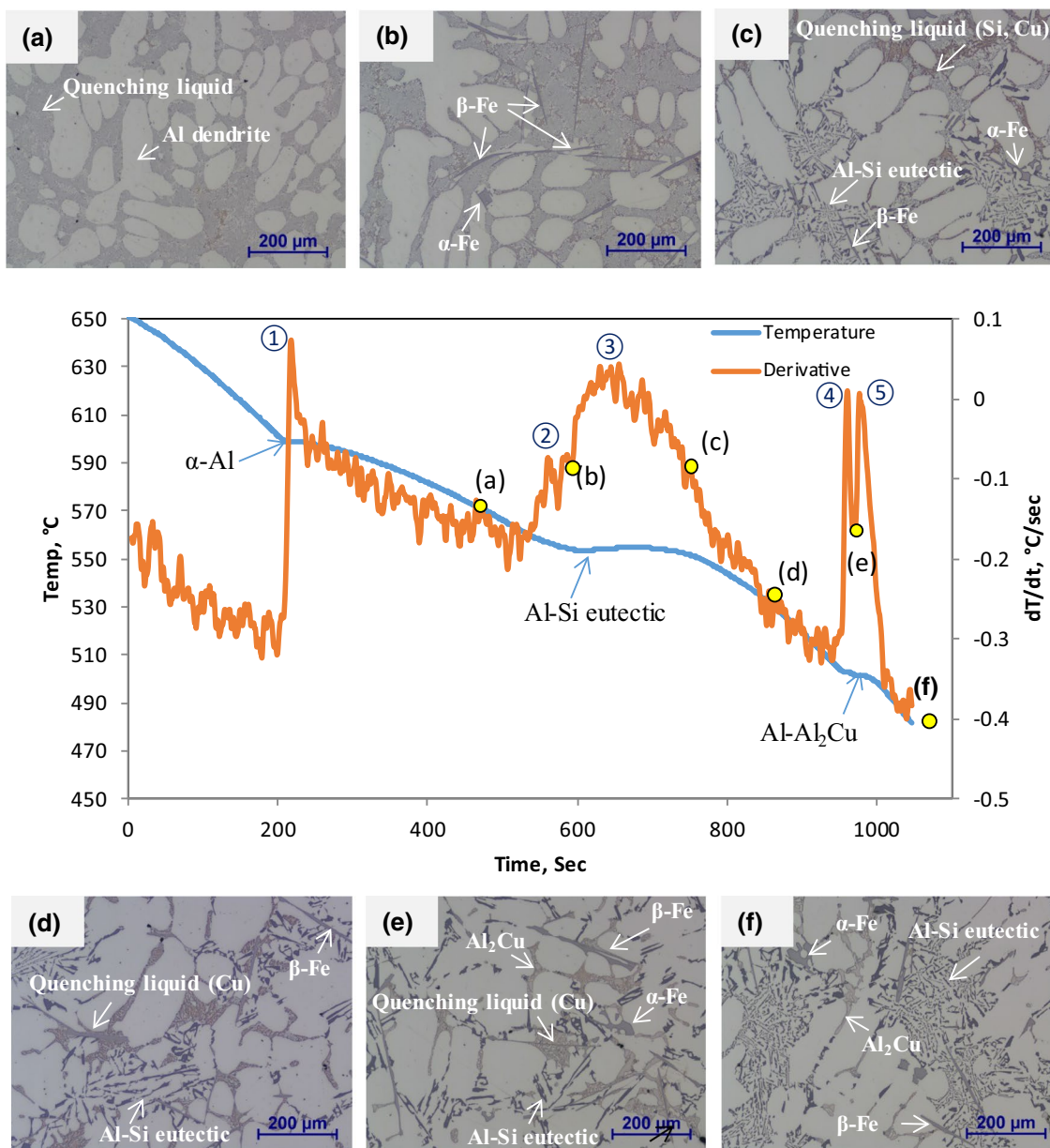


Fig. 2 Solidification curve (in blue) and its first derivative (in red) for standard alloy and optical micrograph after interrupted quenching at different temperatures: **a** 560 °C, **b** 554 °C, **c** 547 °C, **d** 520 °C, **e** 502 °C and **f** full solidification

primary aluminium dendrites at peak 1. Nucleation temperature, read on Fig. 2, of α -Al is about 603 °C. Figure 2b shows that the iron-intermetallic phase, β - Al_3FeSi , was mostly found in the sample quenched at 554 °C, while little α -Fe phase was detected, therefore, Peak 2 in first derivative curve mainly indicates the nucleation temperature of iron-intermetallic phases, either α or β , at 560 °C. In the sample quenched at 547 °C (Fig. 2c), eutectic Si and α/β -Fe phases were observed. As some water-quenched structures, which contain Si and Cu elements, could still be found, the formation of eutectic Si phase was not completely finished, and the Al_2Cu phase has not yet precipitated. Therefore, Peak 3 indicates the main Al–Si eutectic reaction. The microstructure of a sample quenched at 520 °C in Fig. 2d reveals that almost all the eutectic silicon phase was formed.

Two reaction peaks (N^o4 and 5) were observed on the first derivative at 505 °C and 502 °C. Peak 4 is related to the nucleation temperature of Al_2Cu phase as confirmed by microstructural study of quenched sample. As seen from the Fig. 2e, Al_2Cu phase was found in the sample quenched at 502 °C but some quenching liquid structure could still be observed.

In order to determine the reaction that occurs in Peak 5, the microstructures in the samples quenched at temperatures immediately before and after peak 4, after peak 5, respectively, have been compared and identified using SEM–EDS in Fig. 3. The Fig. 3a–c show the SEM images of samples from point d, e and f in Fig. 2, respectively. The chemical

compositions at different points marked 1 to 5 are given in Table 2.

In the sample quenched before Peak 4, the quenching liquid structure was detected (as shown in Fig. 3a), the EDS analysis revealed that this structure in point 1 contains some Mg, Al, Si and Cu with concentration of Mg and Cu between 3 to 4 at% and 11 to 12 at%, respectively. Figure 3b and c show the microstructures of sample quenched after Peaks 4 and 5, respectively, with the formation of a white phase identified by EDS at points 3 and 4. According to the chemical composition given by the spectrum analysis (Table 2), this phase corresponds to the Al_2Cu phase [21]. Thus, Peak 4 in Fig. 3 indicates the formation of Al_2Cu phase at 505 °C. In the sample quenched after Peak 5, EDS analysis revealed that the structure in point 5 (see Fig. 3c) consists of Mg, Al, Si and Cu, and that its stoichiometry corresponds to the $\text{Al}_5\text{Mg}_8\text{Cu}_2\text{Si}_6$ phase [22].

However, in the sample quenched after Peak 4, some liquid structures (point 2 in Fig. 3b) still exist and also contain some Mg, Al, Si and Cu with similar chemical composition as point 1 in Fig. 3a. Thus, the comparison of the microstructures of samples quenched after Peak 4 and Peak 5 (Fig. 3b and c), and the presence of significant Mg and Cu in the remaining liquid of sample quenched after Peak 4 allow to conclude that Peak 5 is associated with the formation of $\text{Al}_5\text{Mg}_8\text{Cu}_2\text{Si}_6$ phase. It should be mentioned that a very small amount of $\text{Al}_5\text{Mg}_8\text{Cu}_2\text{Si}_6$ phase was also observed in the sample quenched after Peak 4 (see the yellow circle in

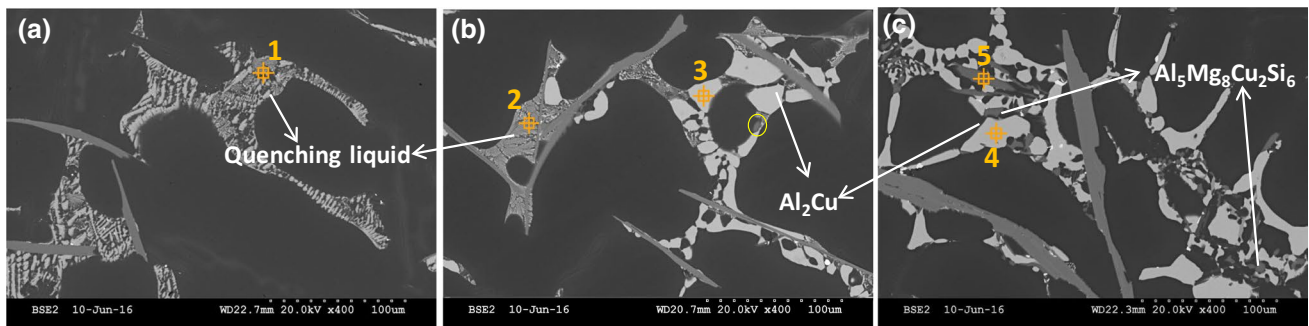


Fig. 3 BSE micrograph of the sample quenched at temperature **a** before peak 4 and immediately after **b** peak 4 and **c** peak 5

Table 2 EDS analysis of the phases in Fig. 3

Sample	Number	Element content (at%)				Identified phase	Measured stoichiometry
		Mg	Al	Si	Cu		
Quenched before peak 4	1	3.10	77.89	6.46	11.68	–	–
Quenched after peak 4	2	3.60	76.50	8.02	11.88	–	–
	3	–	71.29	1.09	27.62	Al_2Cu	$\text{Al}_{2.5}\text{Cu}$
Quenched after peak 5	4	–	70.98	1.35	27.67	Al_2Cu	$\text{Al}_{2.5}\text{Cu}$
	5	36.38	20.73	34.31	8.59	$\text{Al}_5\text{Mg}_8\text{Cu}_2\text{Si}_6$	$\text{Al}_{4.8}\text{Mg}_{8.4}\text{Cu}_2\text{Si}_8$

Fig. 3b). The proximity between the two reaction Peaks for the formation of Al_2Cu and $\text{Al}_3\text{Mg}_8\text{Cu}_2\text{Si}_6$ phases and the uncertainty in the interrupted quenching temperature may be an explanation.

A fully solidified structure was observed in the sample quenched after Peak 5 (i.e. at 480 °C), see Fig. 2f, consequently, the solidification process can be assumed to terminate between 502 and 480 °C, and more precisely around 496 °C according to the Fig. 2(end of Peak 5).

3.1.2 Effect of Fe and Mn on the Formation of Intermetallic Compounds

Figure 4a shows the temperature derivatives measured during solidification for standard alloy and high-Fe/Mn alloy. Figure 4b and c show the microstructures of the quenched samples at 560 °C (i.e. the temperature immediately after the arrowed Peak) for the two alloys. Only Al dendrites and quenching liquid structures were observed in standard alloy. However, in high-Fe/Mn alloy, which has 0.8 wt% Fe and 0.51wt% Mn, both α and β phases were observed prior to the eutectic Si as shown in Fig. 4c. Comparing

the microstructures of the standard and high-Fe/Mn alloy quenched at 560 °C in Fig. 4b and c, it can be concluded that the increase of Fe and Mn content shifts the precipitation sequence of α and β phases toward a higher temperature. The Peak (dotted arrow in Fig. 4a), which represents the formation of iron-intermetallic in standard alloy is less significant and occurs at a lower temperature than in the alloy with high Fe and Mn addition (i.e. high-Fe/Mn alloy). In addition, the temperature of nucleation of α -Al dendrite is observed to increase from 600 to 605 °C for both studied alloys, and the reason will be discussed later.

3.2 Microstructure Examination

The typical microstructures obtained from standard and high-Fe/Mn alloy in the cross section of samples are shown in Fig. 5. Platelet eutectic Si particles, needle-like β - Al_3FeSi and Al_2Cu phase can be observed in both alloys; however, compared with the standard alloy, the high-Fe/Mn alloy shows more iron-intermetallics, i.e. α - $\text{Al}_{15}(\text{Fe,Mn})_3\text{Si}_2$ and β - Al_3FeSi .

Fig. 4 a Temperature derivatives measured from the melts with different Fe/Mn addition. Microstructures of samples quenched at 560 °C for b Standard alloy and c High Fe/Mn alloy

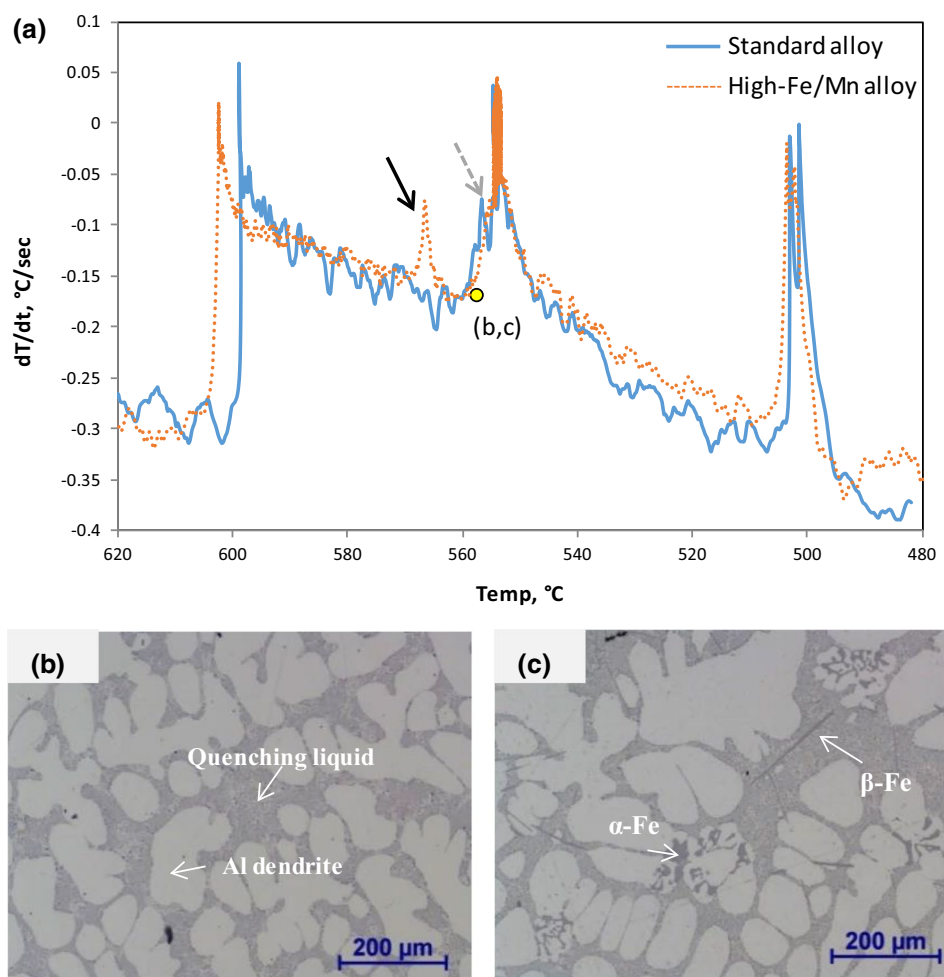
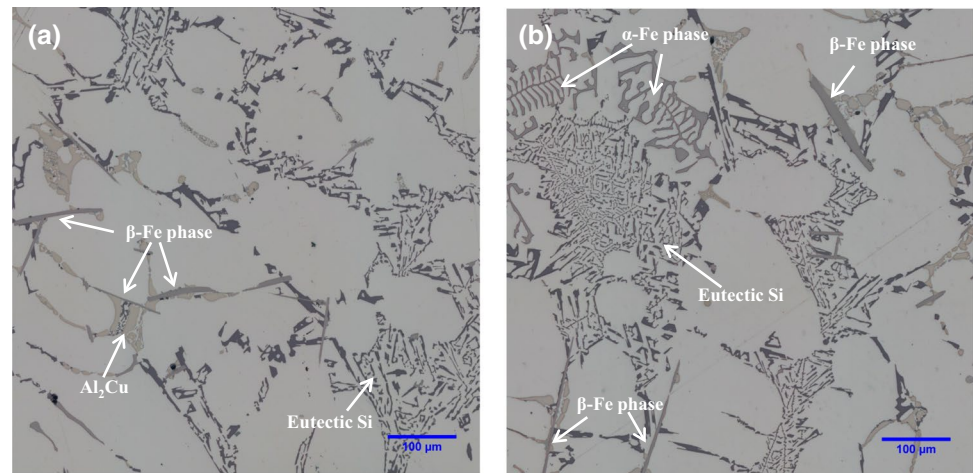


Fig. 5 Optical microstructures of sample for **a** standard and **b** high-Fe/Mn alloy



Secondary dendrite arm spacing (SDAS) measurements were performed on the two alloys, and the result shows that the average size of SDAS decreased from 66.5 to 63.0 μm when the Fe and Mn content increased from 0.49% and 0.13% to 0.80% and 0.51%, respectively.

3.2.1 Porosity Characterization

Figure 6 shows 3D renderings of pores in the two alloys at a voxel size of 3.14 μm ; Fig. 6a and b refer to the standard and high-Fe/Mn alloy, respectively. The measured pores characteristics for the two different Al-Si-Cu alloys are provided in Table 3.

As seen from the Table 3, there is no obvious difference between the average size of pore in both alloy, and the total volume fraction of pore in high-Fe/Mn (3.0%) is higher than in standard alloy (2.1%). However, a large macro shrinkage (see blue arrow in Fig. 6b), was found in the studied sample with high-Fe/Mn content, which occupies 33% of the total pore volume fraction. Removing this largest shrinkage from the sample with high-Fe/Mn (see Fig. 6c), the volume fraction of pore becomes 2.0% which is similar to the standard alloy (2.1%).

In this work, a higher pore density is observed in high-Fe/Mn alloy compared with standard alloy. The distributions of pores as a function of Feret diameter in standard alloy and

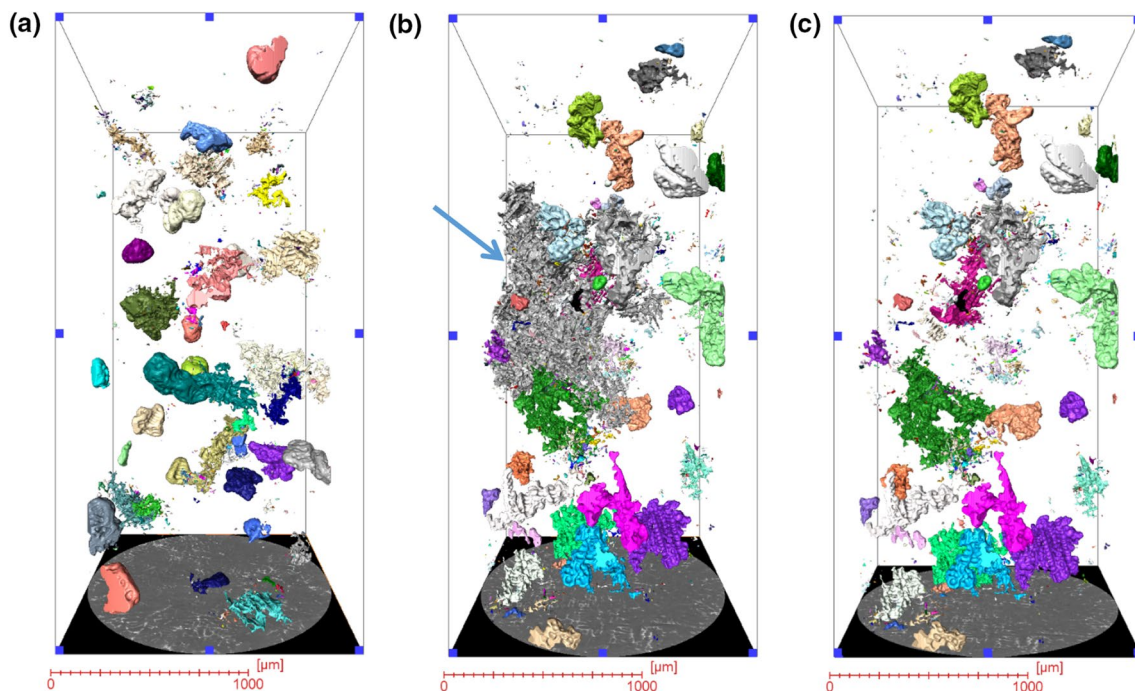
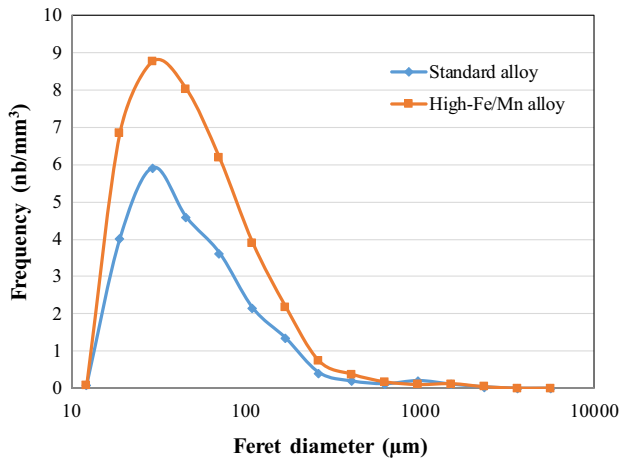


Fig. 6 3D rendering of pores for **a** standard alloy sample, **b** high-Fe/Mn sample and **c** high-Fe/Mn sample without the largest shrinkage

Table 3 Porosity characteristics in the studied standard alloy and high-Fe/Mn alloy

Alloy	Fe	Mn	Volume fraction (%)	Feret diameter (μm)		Density (particles/ mm^3)
				<i>Av</i>	<i>Max</i>	
Standard	0.49	0.13	2.1	66	2121	27.8
High-Fe/Mn (with largest shrinkage)	0.80	0.51	3.0	66	4698	37.7
High-Fe/Mn (without largest shrinkage)			2.0	61	2481	

**Fig. 7** Size distribution of pores in frequency for standard alloy and high-Fe/Mn alloy

high-Fe/Mn in Fig. 7 show that increasing Fe/Mn content introduces more pores in the range of 10–250 μm .

3.2.2 Fe-Rich Intermetallics

The effect of Fe, Mn content on the formation of the Fe-rich intermetallic compounds was also studied in the two experimental alloys through the 2D and 3D observation. Due to the similar gray value of $\alpha\text{-Al}_{15}(\text{Fe}, \text{Mn})_3\text{Si}_2$ and $\beta\text{-Al}_3\text{FeSi}$ phase, the α - and β -Fe phase cannot be distinguished by image segmentation, thus the Fe-rich intermetallics mentioned in this section include both α - and β -phase.

The size, i.e. average and maximum Feret diameter, volume fraction of Fe-rich intermetallics are listed in Table 4. One can note that when the Fe and Mn content increased

from 0.49% and 0.13% to 0.80% and 0.51%, the volume fraction of Fe-intermetallics increased from 2.36 to 3.85%. The average and maximum length of the Fe-intermetallics also increased as the Fe and Mn content increased.

Typical 3D volume rendering of individual $\beta\text{-Al}_3\text{FeSi}$ and $\alpha\text{-Al}_{15}(\text{Fe}, \text{Mn})_3\text{Si}_2$ intermetallic particles are shown in Fig. 8a and b. The surface of the particles were colored according to the local values of the mean curvature H : red color corresponds to high positive curvatures ($H > 0$), green color corresponds to flat surface ($H = 0$), and cyan color corresponds to local pit or groove ($H < 0$). As shown in Fig. 8a, thin platelets shape β -Fe phase (appearing as needles-like in 2D observation) can be clearly observed, the interfaces with large positive mean curvature correspond to the edge of the plate for $\beta\text{-Al}_3\text{FeSi}$. As seen in Fig. 8b, The $\alpha\text{-Al}_{15}(\text{Fe}, \text{Mn})_3\text{Si}_2$ is a complex and interconnected network, and it exhibits the convoluted three-dimensional branched structure, which usually appears as Chinese-script in 2D observation. The complex 3D structure of $\alpha\text{-Al}_{15}(\text{Fe}, \text{Mn})_3\text{Si}_2$ phase shows high positive curvatures (red color) concentrated in the corner, and more cyan color which corresponds to local pit or groove.

The 3D rendering of all Fe-intermetallic particles in the large volume (1.24 mm^3) of the standard alloy and high-Fe/Mn alloy are also shown in Fig. 8c and d, respectively; they are colored with the mean curvature values at the interface location. Complex network structures are present in the volume for both alloys.

In order to analyze the amount of α -Fe and β -Fe in the two studied alloys, Fig. 9 presents the evolution of Mean and Gaussian curvature using probability density distributions for the Fe-intermetallics shown in Fig. 8a–d, respectively. The range of Mean and Gaussian curvature values reflects

Table 4 Hard inclusions characteristics in the studied standard alloy and high-Fe/Mn alloy

Alloy	Fe-rich intermetallics		Al_2Cu		Eutectic Si				
	Feret diameter (μm)	Volume fraction (%)	Feret diameter (μm)	Volume fraction (%)	Feret diameter (μm)		Surface area fraction (%)		
					<i>Av</i>	<i>Max</i>			
Standard	13.7	1073	2.36	25.0	1018	1.68	6.0	185	7.46
High-Fe/Mn	22.7	1487	3.85	25.5	961	1.59	6.5	241	7.56

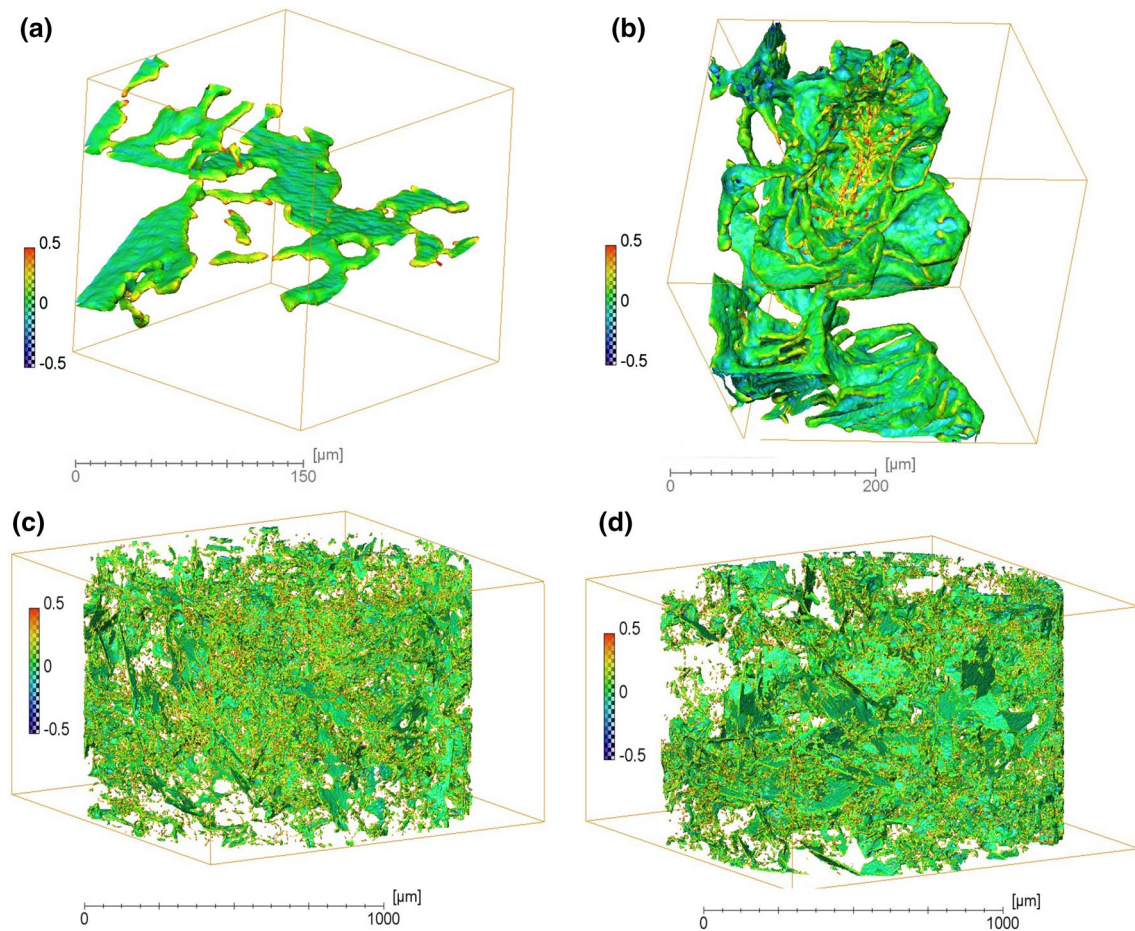


Fig. 8 3D rendering of intermetallics for **a** β -Fe, **b** α -Fe, Fe-intermetallics phases in **c** standard and **d** high-Fe/Mn alloy; the colour represents the mean curvature values at the interface location

the different possible morphologies of the interfacial surface. In H–K, the distinction between α -Fe and β -Fe is readable (see Fig. 9a and b). For β -Fe phase, most of the curvature values can be observed in the positive–positive and positive–negative quadrant of the coordinate system, which indicates the presence of more near-spherical shapes and convex saddle regions. However, α -Fe shows more varied morphologies, there are more points for α -Fe particle located in the zone ($H < 0$; $K > 0$) which corresponds to concave interfaces on the intermetallic side, and there are more trough shapes ($H < 0$; $K = 0$) in α -Fe than β -Fe. On the other hand, as seen in Fig. 9c and d, the peak of the distribution for both alloys lies at a slightly positive mean curvature, it is thus difficult to observe the distinction between standard and high-Fe/Mn alloy.

The result shows that the difference in β -phase fraction does not seem significant enough to be detected although the distinction between α - and β -phase curvatures is clear when they are taken apart. In addition, a small volume which contains the same volume of Fe-intermetallics for

both studied alloys was selected and analyzed for standard and high-Fe/Mn alloys, the distribution of mean and Gauss curvature of all Fe-intermetallics also show no strong difference between standard alloy and high-Fe/Mn alloy.

3.2.3 Al_2Cu and Eutectic Si Characterization

Figure 10 shows a 3D rendering of the Al_2Cu phase in the studied standard alloy at a voxel size of 1.1 μm . The different colors indicate unconnected particles within the studied volume. The complex 3D-structure and the interconnectivity can be seen quite clearly. The measured Al_2Cu characteristics for the two alloys are provided in Table 4. The results show that increasing the Fe and Mn content has no significant effect on the formation of Al_2Cu phase.

The Si phase could not be revealed by Lab-CT as Al and Si have close atomic numbers hence similar X-ray attenuation [15], thus the 2D characterization for Si phase was performed by optical microscopy. In the present work, the platelet eutectic Si particles can be observed from the two

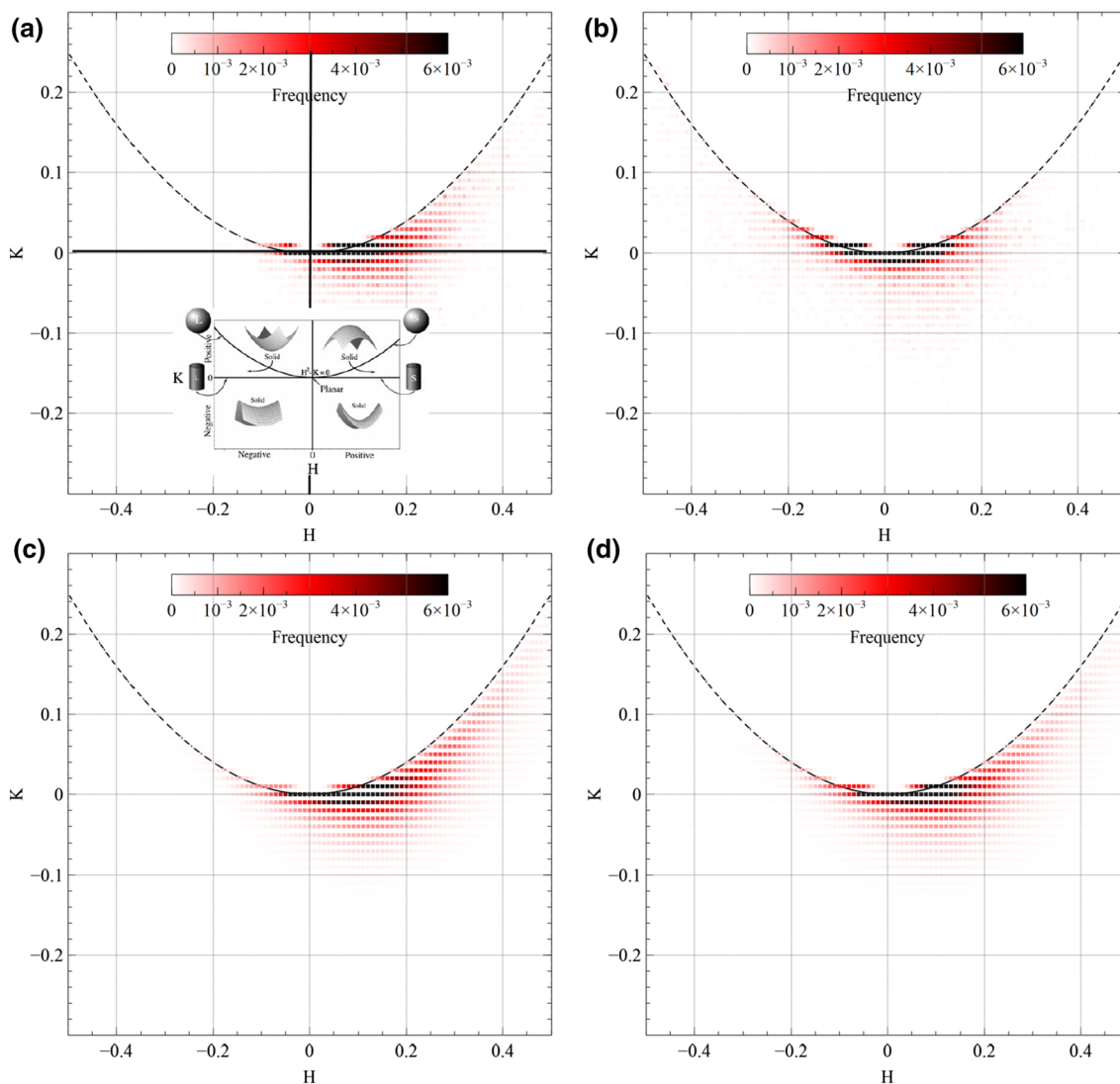


Fig. 9 a, b, c and d show the probability density distributions in H–K– coordinates for the microstructures shown in Fig. 8 a, b, c and d, respectively, i.e. for a β -Fe, b α -Fe, Fe-intermetallics phases in c standard and d high-Fe/Mn alloy

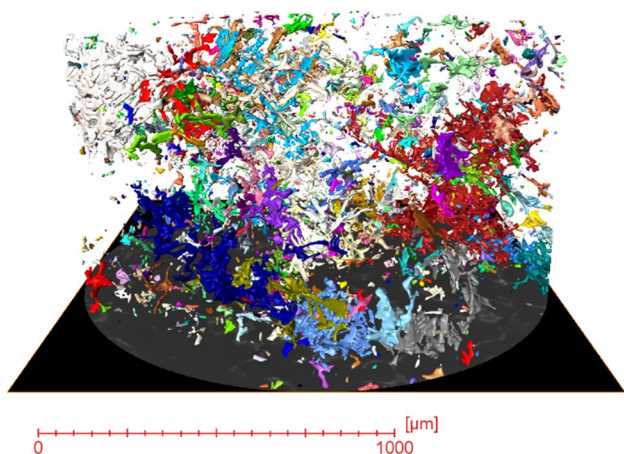


Fig. 10 3D rendering of Al_2Cu phase for standard alloy

studied samples (see Fig. 5), and the quantitative metallography analysis shows that the surface fraction of eutectic Si is 7.5% and 7.6% in the standard and high-Fe/Mn alloys respectively, and there is no significant difference for the morphology of eutectic Si between the two alloys (see Table 4).

3.3 Mechanical and Fracture Behaviour

Mechanical properties of the $AlSi7Cu3$ alloys with different Fe/Mn contents are presented in Fig. 11a. The average elongation (EI%) slightly decreased from 0.32 to 0.29% while the yield strength slightly increased with the increase in Fe/Mn content. However, no obvious change was observed for the ultimate tensile strength (UTS). Specifically, the variation was from 99 to 102 MPa for the yield strength (0.05% offset)

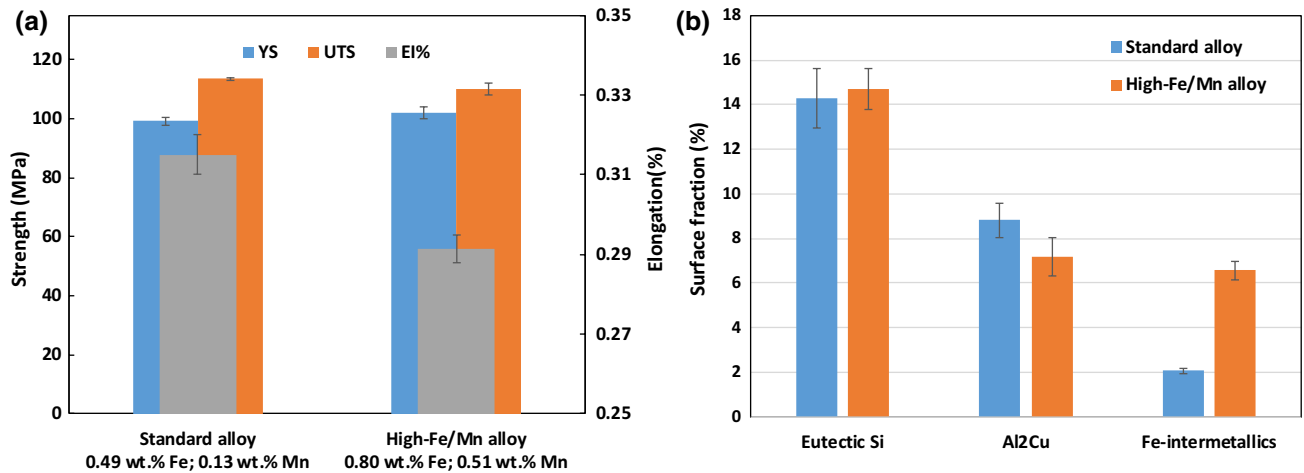


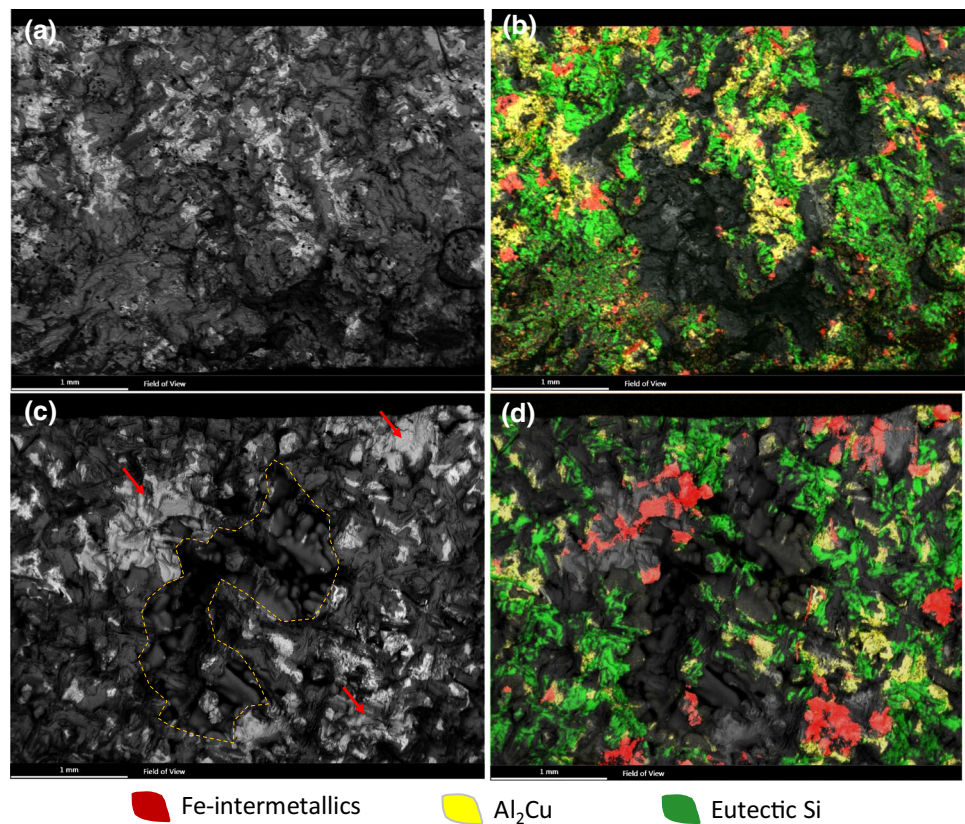
Fig. 11 **a** The tensile properties of the as-cast Al–Si–Cu alloys with different Fe/Mn contents (YS: yield strength; UTS: ultimate tensile strength; El: elongation); **b** Surface fraction of hard inclusions in the fracture surface for standard and high-Fe/Mn specimen

and from 113 to 112 MPa for the UTS when the Fe and Mn content increased from 0.49% and 0.13% (Standard alloy) to 0.80% and 0.51% (High-Fe/Mn alloy).

Besides, fracture analysis using SEM–EDS has been performed on both alloys. The analysis area, which is nearly 12mm², includes the whole thickness of the tensile specimen and represents $\frac{3}{4}$ of the total tensile fracture

surface. BSE images of the fracture surface for standard specimen and high-Fe/Mn specimen are shown in Fig. 12a and c. The corresponding X-ray elemental mappings of the fracture surface for both specimens are shown in Fig. 12b and d. The eutectic Si particles, Al₂Cu particles and iron-intermetallics are clearly observed in the fracture surface and they occupy a large area fraction

Fig. 12 BSE images of the fracture surfaces and corresponding X-ray mapping images showing the distribution of hard inclusions (eutectic Si, iron-intermetallics, Al₂Cu phases) of **a, b** standard and **c, d** high-Fe/Mn specimen



of the fracture surface for both specimens. It is interesting to notice that the fracture surface of the high-Fe/Mn specimen shows comparatively more iron-intermetallics than standard specimen. Broken α -phases (red arrows in Fig. 12c), which appear as convoluted branched structure in 3D, are seen as massive platelets whose nature is confirmed by the X-ray elemental mapping in Fig. 12d.

Indeed, a quantitative chemical composition analysis has been performed on the fracture surface for the two specimens using SEM–EDS. It should be noted that there exists some areas that cannot be detected by EDS because of shadowing effects in the rough fracture surface, and because it is difficult to acquire all spatial information of a large area in one map. Besides, for the high-Fe/Mn specimen, there is a large shrinkage porosity (dotted yellow circled in Fig. 12c) which also occupies nearly 14.5% of the total analysis area. The surface fraction of iron-intermetallics (2%–7%), Al_2Cu phase (6.35%–9.57%) and eutectic Si (12.98%–15.6%) in the fracture surface for both specimens is shown in Fig. 11. As compared with the volume fraction of iron-intermetallics (2.36%–3.85%), Al_2Cu phases (1.59%–1.68%) and surface fraction of Si phase (7.46%–7.56%) in both alloys (see Table 4), we can conclude that the fraction of hard inclusions is higher in the fracture surface than in the volume of specimen for both cases. This implies that cracks and final fracture are more prone to occur at hard inclusions than in Al dendrites.

In addition, pores also play an important role on controlling the tensile behaviour of Al–Si alloy [15]. In the present work, quantitative analyses of the pores surface fraction on the fracture surface was systematically performed on the broken tensile specimens for both alloys. For the standard alloy, the pores occupy 1.5%, 7.0% and 9.1% of the fracture surfaces in the three broken specimens respectively whereas they occupy about 12.2%, 15.3% and 17.2% of the fracture surfaces in the specimens with high-Fe/Mn content.

4 Discussion

4.1 Phase Formation in Al–Si–Cu Alloy

The first derivative of the cooling curve could clearly reveal peaks which correspond to the phase formations during the solidification. In this work, based on the microstructural observation of the quenched and fully solidified samples, the possible reactions corresponding to each individual peak were identified and all possible solidification reactions and sequences for the studied standard alloy were summarized in Table 5.

The solidification of the studied Al–Si–Cu alloy can be described as follows:

- (1) A primary α -aluminium dendritic network forms between 600 and 611 °C. The exact temperature depends mainly on the amount of Si and Cu in the alloy. As shown in Fig. 4a, the temperature of nucleation of α -Al dendrite increases from 600 to 604 °C when the Si and Cu content decreases from 7.66 wt% and 3.67 wt% (standard alloy) to 7 wt% and 3.45 wt% (high-Fe/Mn alloy), respectively. This is in good agreement with the results reported by [23] and [24]. When the Si and Cu content increases in Al–Si–Cu alloys, the nucleation temperature of α -aluminium decreases.
- (2) At approximately 568 °C, the iron-intermetallics, including α -Fe and β -Fe phases, begin to precipitate in the high Fe/Mn level alloys. Experimental studies have demonstrated that the formation of the intermetallic compounds is influenced by the Fe and Mn content. At low Fe/Mn level (standard alloy), the temperature for precipitation of iron-intermetallics is reduced to 560 °C.
- (3) At approximately 556 °C, the Al–Si eutectic phase begins to precipitate.
- (4) At approximately 505 °C, the Al_2Cu phase forms.

Table 5 Reactions occurring during solidification of studied Al–Si–Cu alloys

Peak	Solidification reactions	Approximate temperature, °C	Temperature calculated by Scheil model, °C
1	(Al) dendritic network	600–611	597
2	Precipitation of α/β -Fe phases	560–568	585–593
3	Precipitation of eutectic Si	556	565
4	Precipitation of Al_2Cu	505	513
5	Precipitation of $\text{Al}_5\text{Mg}_8\text{Cu}_2\text{Si}_6$	502	510
	End of solidification	496	485*

*Calculated by equilibrium condition

- (5) At approximately 502 °C, a fine $\text{Al}_5\text{Mg}_8\text{Cu}_2\text{Si}_6$ phase forms. This phase grows close to the eutectic Al_2Cu phase.
- (6) At approximately 496 °C, the alloy is fully solidified.

In the present work, CALPHAD modelling of the multicomponent Al-Si-Cu system was also carried out using Pandat software. The calculated equilibrium phase diagram on the cross section of the studied standard Al-Si-Cu alloy is shown in Fig. 13. The solidification behaviour calculated by Scheil model is shown in Table 5. The transformation temperatures measured by interrupted quenching test show the same tendency as the results calculated by Scheil model in Pandat software.

The temperature of nucleation of α -Al dendrites calculated by Scheil model is close to that of experimental observation, while there exists a larger difference in the temperature for α/β -Fe phases precipitation, i.e. a delay in the formation of α/β -Fe phases is observed in experimental data as compared to the calculation. This difference may be due to the nucleation of α/β -Fe phases that requires high undercooling during solidification [25]. It also should be noted that the temperatures at which reactions occur are influenced by the cooling rate [26]. Although the cooling rate for the thermal analysis used in the present work is slow (0.13 °C/s), it is still faster than the critical cooling rate for equilibrium solidification of Al-Si alloy [27]. Besides, the sensitivity of thermocouple which was used in the study may also affect the phase transformations temperatures acquisition. The range of the different phase transformations temperatures of Al-Si-Cu alloy was investigated in the literature. A temperature range from 575 to 590 °C corresponds to the precipitation of $\alpha + \beta$ phases as detected during solidification of an A319.1 alloy (containing 0.62 wt% Fe, 0.36 wt% Mn) at

a cooling rate of 0.6 °C/s as reported by Bäckerd et al. [28] who suggested that the precipitation of α - $\text{Al}_{15}\text{Mn}_3\text{Si}_2$ occurs possibly together with β - Al_5FeSi . However, the precipitation of α - $\text{Al}_{15}\text{Mn}_3\text{Si}_2$ was not observed by Samuel et al. [29] presumably because of the lower Mn content (0.14 wt%) of the alloy they used. Samuel et al. [29] also reported that precipitation temperature of the eutectic Si is 562°C, and that at 510 °C the Al_2Cu phase begins to precipitate, which is similar to the results of the present work.

In addition, from Fig. 13, it can be seen that α phase should form earlier than β phase according to the calculated phase diagram, which was hard to distinguish from the previous experimental observations. The reason for this may be due to the Mn content of only 0.13 wt% in the standard alloy so that the amount of α phase in the studied standard alloy is very low, and the precipitation range of α phase is narrow (see red arrow in Fig. 13) in the diagram.

4.2 The Effect of Fe and Mn Content on Microstructures

From the results shown in Table 4, it is clear that, with the increase of Fe and Mn content, the total amount and size of the Fe-intermetallics is increased. Comparing the microstructures of quenched samples for these two studied alloys in Fig. 2, both α and β phases were observed in the fully solidified samples of the two alloys. However, α and β phases observed in the sample with higher Fe and Mn form earlier at a higher temperature; increasing the Fe and Mn content shifts the precipitation sequence of the α and β phases toward a higher temperature. Similar results were reported by [14]. Thus, the longer time available for growth of iron-intermetallic at high Fe alloy may also explain the larger size of Fe-intermetallics present.

Besides, three-dimensional reconstructions of individual α and β phases have also been made using CT imaging in this work. As shown in Fig. 8a and b, α and β phases form with the complex three-dimensional branching structure and platelet morphology, respectively. Such results are in good agreement with several published papers [6, 30, 31], which reported that α - $\text{Al}_{15}(\text{Fe}, \text{Mn})_3\text{Si}_2$ and β - Al_5FeSi phases appear as Chinese script and needles in two-dimensional optical micrographs, respectively.

The curvature distribution for individual particles of α and β phase can reflect the topological difference between the two phases. However, as previously shown in Fig. 9c and d, the volume ratio of α to β phases when considering not individual particles but iron intermetallic phases as a whole in the analyzed volume for the standard and high Fe/Mn alloys cannot be estimated by comparing the characteristics of curvature distribution between individual in the two alloys.

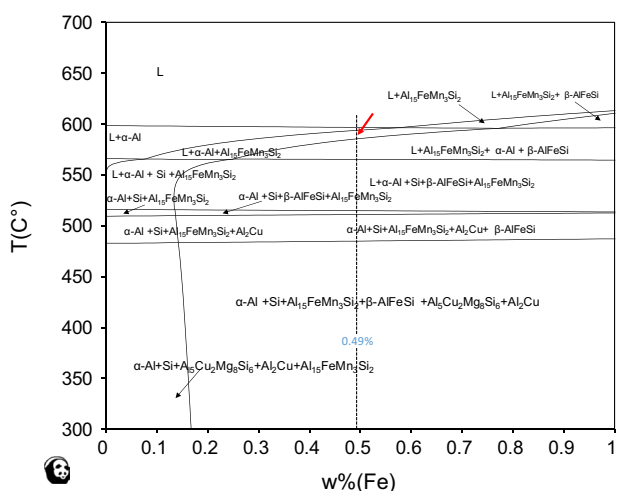


Fig. 13 The cross section of equilibrium phase diagram of the studied standard Al-Si-Cu alloy calculated by Pandat software

The difference between α and β phase taken individually (Fig. 8a and b) are the recessed regions (zone with $H < 0$) in α phase that are not found in β phase. However, it is hard to see the difference between α and β phase in the H–K distributions in volume in the standard and high Fe/Mn alloys (Fig. 8c and d). There are two possible reasons: (1) β phase particles in the standard alloy are also interconnected in 3D which will give rise to the hollow zones with $H < 0$, and it is difficult to distinguish from the specific-zone with $H < 0$ of α phase. Terzi et al. [32] observed the formation of β -Al₅FeSi intermetallic plates during solidification of Al–Si casting alloys using high-energy synchrotron X-rays. They reported that the β -Al₅FeSi intermetallic forms in complex interconnected three-dimensional plates. Puncreobutr et al. [33] also studied the formation of β phases and showed that the platelets eventually form branches. (2) β phase particles are still present and with a larger size in high Fe/Mn alloy than in the standard alloy, thus, it will show out in the H–K density plot distribution.

However, it is also possible to distinguish α and β phases by naked eye from 2D optical images due to the shape of Chinese script-like and plate-like for α -phase and β -phase, respectively. The number of α -phase and β -phase particles in a selected large area (5.05 mm²) in both alloys were counted. The standard alloy showed 2 α -phase particles and 32 β -phase particles, whereas the high Fe/Mn alloy (i.e. high ratio of Mn and Fe) showed 11 α -phase particles and 38 β -phase particles. Thus, the ratio of α to β phase increases as the amount of Fe and Mn increases because part of the Fe and Mn in the melt precipitates as a new Chinese script-like phase (α -Al₁₅(Fe,Mn)₃Si₂), prior to the formation of eutectic Si. This is clearly observed in the quenched sample in Fig. 4c. Therefore, Mn is expected to promote the more compact α phase [14]. However, in the present case, the Mn content was not enough to suppress the β phase formation. The 3D rendering (Fig. 8d) clearly shows that β phase is present and larger than in the standard alloy.

In addition, the effect of Fe/Mn content on the pores formation was also studied in this work. Large pores (Feret diameter > 200 μ m) occupy approximately 99% of the total volume fraction of the pores population in the analysis zone (83.5 mm²) of both alloys. This can be explained by the low cooling rate (0.13 °C/s). At low solidification rate, hydrogen has more time to diffuse into the interdendritic spaces of the partially solidified metal [11], resulting in more large pores. The largest pore (see arrow in Fig. 6b) in the high-Fe/Mn sample is a localized shrinkage-porosity defect. Taylor et al. [12, 34] named this type of shrinkage whose size is above the general background porosity level as “extended defect”, and reported that they are always developed at high iron concentrations due to the poor casting condition that results from the large amount of binary β -Al₅FeSi eutectic forms. The tomographic image of high-Fe/Mn sample was analyzed

slice by slice, more β -Fe intermetallics could be observed around this largest shrinkage than elsewhere in the sample. However, it should be noted that the large shrinkage could be distributed randomly in the sample and the volume fraction of porosity for both studied alloys becomes close when removing the largest shrinkage from the high Fe/Mn sample. Besides, there is only one such shrinkage-porosity that was observed in the sample. Thus, there is insufficient evidence indicating that the amount of porosity is significantly enhanced by increasing the Fe and Mn content from 0.49% and 0.13 (Standard alloy) to 0.80% and 0.51% (High-Fe/Mn alloy) in the present work. There are no studies proving the influence of Fe-intermetallics on the germination of the pores except that of Puncreobutr [33] who only give the pores formation temperature. Thus, whether the pores nucleated on the Fe-intermetallics or not should be further studied in high resolution in-situ tomography experiments.

In addition, it was also found that the increase of iron-intermetallics resulting from higher Fe/Mn content can induce more and smaller pores (see Fig. 7). Some researchers [35, 36] claimed that the pore formation is always linked with the β -Al₅FeSi, as Fe leads to the generation of β -Al₅FeSi platelets, which in turn, increase shrinkage by physically blocking interdendritic feeding, thus the reason of formation of these discrete individual small pores in the present work is maybe due to the large amount of β -Al₅FeSi acting as potential sites for pore nucleation. On the other hand, Puncreobutr et al. [33] reported that larger pores were observed to nucleate before the intermetallics during in-situ solidification of an A319 alloy at 0.36 °C/s, and that they change shape when they come into contact with intermetallics. Besides they observed a number of smaller pores that appear to nucleate after the Fe-intermetallics, therefore, it can be reasonably assumed that Fe-intermetallics could even limit pore growth.

4.3 Effect of Fe and Mn Content on the Tensile Behaviour

The experimental results have confirmed that YS and UTS are not very sensitive to the Fe/Mn content in the two studied alloys. This is in agreement with the results reported by [37]. The slightly decreased elongation can be attributed either to more numerous iron intermetallics or to higher volume fraction of pores in high-Fe/Mn alloy compared to standard alloy. [15] reported that pores can generate enough strain localization zones for crack initiation in monotonic tensile. Thus we can conclude that the increase of iron-intermetallics resulting from higher Fe/Mn content does not have a marked detrimental effect on the properties in monotonic tension of the present alloys that both contain a high volume fraction of large pores (Av. Feret diameter ~ 60 μ m; volume fraction of pores ~ 2%).

Fracture surfaces examination with SEM–EDS has helped finding the features responsible for crack growth and final fracture during the tensile loading. Surface fractions of hard inclusions, i.e. Si particles, iron-intermetallics and Al_2Cu phases, in the fracture surface were higher than their volume fractions for both alloys, which suggest that the hard inclusions play an important role in the tensile behaviour. The reason for this may be due to the stress concentration enhancement as a result of the presence of 3D branching structure of Fe-intermetallics and Al_2Cu particles, and platelet morphology of eutectic Si particles. This stress concentration could become critical for crack nucleation especially when hard inclusions are close to a large pore. As reported in [38–40], the cracks growth are prone to occur along the hard inclusions rather than in Al matrix in a DC Al–Si–Cu alloy under monotonic loading; this is due to the higher elastic modulus of eutectic Si particles (~ 185 GPa), iron-intermetallics and Al_2Cu phases (~ 126 GPa) as compared to aluminium matrix (~ 70 GPa).

In terms of the different effect of the α and β phases on the mechanical properties Al–Si–Cu alloy, several researchers [40, 41] reported a deleterious effect of the brittle $\beta\text{-Al}_5\text{FeSi}$ on crack initiation in high-Fe Al–Si–Cu alloys. However, Caton et al. [42] reported that the initiation of fatigue cracks can also occur on $\alpha\text{-Al}_{15}(\text{Fe},\text{Mn})_3\text{Si}_2$ phase. This apparent contradiction of the literature may be due to the fact that, as shown in the present study, the β phase network in 3D differs little from that of α phase. As shown in Fig. 12c, three large $\alpha\text{-Al}_{15}(\text{Fe},\text{Mn})_3\text{Si}_2$ particles were observed in the fracture surface of high-Fe/Mn specimen. α -Fe phases have similar curvature distribution as β -Fe phases hence probably similar stress concentration effect, which could explain that the two phases are both potential initiation sites for cracks.

5 Conclusions

In this work, the evolution of microstructures and the solidification reaction and sequence of two studied AlSi7Cu3 alloys (standard alloy and high-Fe/Mn alloy) were investigated by thermal analysis and interrupted quenching test. 2D and 3D metallographic and image analysis have been performed to measure the microstructural changes occurring at different Fe and Mn levels. Monotonic tensile tests were performed to assess the influence of these microstructural changes upon mechanical properties. The following conclusions are highlighted:

- (1) Increasing the Fe/Mn level shifts the precipitation sequence of the $\alpha + \beta$ phases toward a higher temperature. For high-Fe/Mn alloy, the majority of $\alpha + \beta$ phases precipitates prior to the eutectic Si. However, for standard alloy (lower Fe/Mn content), the majority

- of $\alpha + \beta$ phases is expected to form at a lower temperature which is close to the eutectic Si precipitation;
- (2) The size, morphology and surface fraction of iron-intermetallics are influenced by the Fe and Mn content, i.e. the size and amount of Fe-intermetallics ($\alpha\text{-Al}_{15}(\text{Fe},\text{Mn})_3\text{Si}_2$ and $\beta\text{-Al}_5\text{FeSi}$ phase) increase with an increase in the Fe–Mn level. Mn additions result in an increased amount of the α -Fe phase, besides, the higher Fe/Mn content can introduce more and smaller pores;
- (3) The three-dimensional morphologies of $\alpha\text{-Al}_{15}(\text{Fe},\text{Mn})_3\text{Si}_2$ and $\beta\text{-Al}_5\text{FeSi}$ intermetallics were revealed by Lab X-ray Computed Tomography (CT). The $\alpha\text{-Al}_{15}(\text{Fe},\text{Mn})_3\text{Si}_2$ and $\beta\text{-Al}_5\text{FeSi}$ particles were observed to have a highly convoluted and thin platelets 3D structure, respectively.
- (4) The mechanical properties of the studied AlSi7Cu3 alloys with low cooling rate were not sensitive to the Fe/Mn content, and the fractography analysis reveals that cracks growth and final fracture under monotonic load are prone to occur through the eutectic Si, Al_2Cu phases and iron-intermetallics.

Acknowledgements The authors wish to thank the ANR (Agence Nationale de la Recherche) MatetPro project INDiANA (ANR-12RMNP-0011) for funding the study on Al–Si alloys, Pierre Osmond from PSA Peugeot Citroën for providing the material of this study and the China Scholarship Council (CSC) for funding the PhD thesis of Zaidao Li. The ISIS4D X-Ray CT platform which has been funded by International Campus on Safety and Intermodality in Transportation (CISIT), the Nord-Pas-de-Calais Region, the European Community and the National Center for Scientific Research is also acknowledged for microtomographic acquisition, and thank the Common Center of Microscopy (CCM) of Lille University for the SEM and EDS. The authors also thank Dr. Dan Luo for her assistance with casting and SEM analysis.

Declarations

Conflict of interest The authors declare that they have no conflict of interest.

References

1. Z. Li, A.M. Samuel, F.H. Samuel, C. Ravindran, S. Valtierra, H.W. Doty, *Mater. Sci. Eng. A* **367**, 96 (2004)
2. J.Y. Hwang, H.W. Doty, M.J. Kaufman, *Mater. Sci. Eng. A* **488**, 496 (2008)
3. S. Jia, P.G. Allison, T.W. Rushing, L. Nastac, in *Advances in the Science and Engineering of Casting Solidification*, ed. by L. Nastac et al. TMS 2015, Orlando, 15–19 March 2015 (Springer, Cham, 2016), pp. 31–36
4. M.A. Moustafa, *J. Mater. Process. Tech.* **209**, 605 (2009)
5. L.A. Narayanan, F.H. Samuel, J.E. Gruzleski, *Metall Mater. Trans. A* **25**, 1761 (1994)

6. C.M. Dinnis, J.A. Taylor, A.K. Dahle, *Scripta Mater.* **53**, 955 (2005)
7. S. Seifeddine, S. Johansson, I.L. Svensson, *Mater. Sci. Eng. A* **490**, 385 (2008)
8. Z. Li, N. Limodin, A. Tandjaoui, P. Quaegebeur, D. Balloy, *Mater. Charact.* **173**, 110919 (2021)
9. Z. Ma, A.M. Samuel, H.W. Doty, S. Valtierra, F.H. Samuel, *Mater. Design* **57**, 366 (2014)
10. S. Seifeddine, I.L. Svensson, *Metall. Sci. Technol.* **27**, 11 (2009)
11. C.M. Dinnis, J.A. Taylor, A.K. Dahle, *Mater. Sci. Eng. A* **425**, 286 (2006)
12. J.A. Taylor, G.B. Schaffer, D.H. StJohn, *Metall. Mater. Trans. A* **30**, 1643 (1999)
13. J.A. Taylor, G.B. Schaffer, D.H. StJohn, *Metall. Mater. Trans. A* **30**, 1651 (1999)
14. L. Lu, A.K. Dahle, *Metall. Mater. Trans. A* **36**, 819 (2005)
15. L. Wang, N. Limodin, A. El Bartali, J.F. Witz, R. Seghir, J.-Y. Buffiere, E. Charkaluk, *Mater. Sci. Eng. A* **673**, 362 (2016)
16. N. Limodin, L. Salvo, E. Boller, M. Suéry, M. Felberbaum, S. Gailliègue, K. Madi, *Acta Mater.* **57**, 2300 (2009)
17. R.W.I. Yarger, F.K.H. Quek, in *Proceedings IEEE International Symposium on Bio-Informatics and Biomedical Engineering*, Arlington, 8-10 November, 2000 (IEEE, Manhattan, 2000), pp. 297–303
18. J. Alkemper, R. Mendoza, P.W. Voorhees, *Adv. Eng. Mater.* **4**, 694 (2002)
19. N.C.W. Kuyjpers, J. Tirel, D.N. Hanlon, S. Van der Zwaag, *Mater. Charact.* **48**, 379 (2002)
20. D. Emadi, L.V. Whiting, S. Nafisi, R. Ghomashchi, *J. Therm. Anal. Calorim.* **81**, 235 (2005)
21. Y. Watanabe, S. Oike, *Acta Mater.* **53**, 1631 (2005)
22. S.G. Shabestari, S. Ghodrat, *Mater. Sci. Eng. A* **467**, 150 (2007)
23. A.A. Canales, J. Talamantes-Silva, D. Gloria, S. Valtierra, R. Colás, *Thermochim. Acta* **510**, 82 (2010)
24. M.B. Djurdjević, S. Manasijević, *Metall. Mater. Eng.* **20**, 235 (2014)
25. F.C.R. Hernandez, J.M.H. Ramírez, R. Mackay, *Al-Si Alloys: Automotive, Aeronautical, and Aerospace Applications* (Springer, Cham, 2017)
26. S.G. Shabestari, M. Malekan, *Can. Metall. Quart.* **44**, 305 (2005)
27. A. Gorny, J. Manickaraj, Z. Cai, S. Shankar, *J. Alloy. Compd.* **577**, 103 (2013)
28. L. Bäckerud, G. Chai, J. Tamminen, *Solidification Characteristics of Aluminum Alloys, Vol. 2: Foundry Alloys* (American Foundrymen's Society, Schaumburg, 1990)
29. F.H. Samuel, A.M. Samuel, H.W. Doty, Factors controlling the type and morphology of Cu-containing phases in 319 Al Alloy (96–30), in *Proceedings of the AFS Transaction 100th Casting Congress and CASTExpo*, vol. 104 (American Foundrymen's Society, Illinois, 1996), pp. 893–902
30. L. Liu, A.M.A. Mohamed, A.M. Samuel, F.H. Samuel, H.W. Doty, S. Valtierra, *Metall. Mater. Trans. A* **40**, 2457 (2009)
31. J.A. Taylor, The effect of iron in Al-Si casting alloys, in *Proceedings of the 35th Australian Foundry Institute National Conference* (Australian Foundry Institute (AFI), Adelaide, 2004), pp. 148–157
32. S. Terzi, J.A. Taylor, Y.H. Cho, L. Salvo, M. Suéry, E. Boller, A.K. Dahle, *Acta Mater.* **58**, 5370 (2010)
33. C. Puncreobutr, P.D. Lee, R.W. Hamilton, A.B. Phillion, *JOM* **64**, 89 (2012)
34. J.A. Taylor, G.B. Schaffer, D.H. StJohn, *Metall. Mater. Trans. A* **30**, 1657 (1999)
35. N. Roy, A.M. Samuel, F.H. Samuel, *Metall. Mater. Trans. A* **27**, 415 (1996)
36. A.M. Samuel, F.H. Samuel, C. Villeneuve, H.W. Doty, S. Valtierra, *Int. J. Cast. Metal. Res.* **14**, 97 (2001)
37. H. Yang, S. Ji, Z. Fan, *Mater. Design* **85**, 823 (2015)
38. Z. Li, N. Limodin, A. Tandjaoui, P. Quaegebeur, J.-F. Witz, D. Balloy, *Mater. Sci. Eng. A* **794**, 139920 (2020)
39. Z. Li, N. Limodin, A. Tandjaoui, P. Quaegebeur, J.-F. Witz, D. Balloy, *Procedia Struct. Integr.* **2**, 3415 (2016)
40. Z. Li, N. Limodin, A. Tandjaoui, P. Quaegebeur, J.-F. Witz, D. Balloy, *Eng. Fract. Mech.* **183**, 94 (2017)
41. J.Z. Yi, Y.X. Gao, P.D. Lee, T.C. Lindley, *Mater. Sci. Eng. A* **386**, 396 (2004)
42. M.J. Caton, J.W. Jones, J.M. Boileau, J.E. Allison, *Metall. Mater. Trans. A* **30**, 3055 (1999)

Publisher's Note Springer Nature remains neutral with regard to jurisdictional claims in published maps and institutional affiliations.